

Exploring the Phase Diagram of the quantum one-dimensional ANNNI model

M. Cea,^{1,2,*} M. Grossi,^{3,†} S. Monaco,^{4,5,‡} E. Rico,^{6,7,8,9,§} L. Tagliacozzo,^{10,¶} and S. Vallecorsa^{3,**}

¹*Max-Planck-Institut für Quantenoptik, Hans-Kopfermann-Str. 1, D-85748 Garching, Germany*

²*Munich Center for Quantum Science and Technology (MCQST), Schellingstr. 4, D-80799 München*

³*European Organization for Nuclear Research (CERN), Geneva 1211, Switzerland*

⁴*RWTH Aachen University, 52062 Aachen, Germany*

⁵*Deutsches Elektronen-Synchrotron (DESY), D-22607 Hamburg, Germany*

⁶*Department of Physical Chemistry, University of the Basque Country UPV/EHU, Box 644, 48080 Bilbao, Spain*

⁷*Donostia International Physics Center, 20018 Donostia-San Sebastián, Spain*

⁸*EHU Quantum Center, University of the Basque Country UPV/EHU, P.O. Box 644, 48080 Bilbao, Spain*

⁹*IKERBASQUE, Basque Foundation for Science, Plaza Euskadi 5, 48009 Bilbao, Spain*

¹⁰*Institute of Fundamental Physics IFF-CSIC, Calle Serrano 113b, Madrid 28006, Spain*

(Dated: March 1, 2024)

In this manuscript, we explore the intersection of Quantum Machine Learning (QML) and Tensor Networks (TNs) in the context of the one-dimensional Axial Next-Nearest-Neighbour Ising (ANNNI) model with a transverse field. The study aims to concretely connect QML and TN by combining them in various stages of algorithm construction, focusing on phase diagram reconstruction for the ANNNI model, with supervised and unsupervised techniques. The model's significance lies in its representation of quantum fluctuations and frustrated exchange interactions, making it a paradigm for studying magnetic ordering, frustration, and the presence of a floating phase. It concludes with discussions of the results, including insights from increased system sizes and considerations for future work, such as addressing limitations in Quantum Convolutional Neural Networks (QCNNs) and exploring more realistic implementations of Quantum Circuits (QCs).

I. INTRODUCTION

QML and TNs are both advanced topics at the intersection of quantum computing and Machine Learning (ML), but they have different focuses and applications. Both QML and TNs involve concepts from quantum mechanics. QML has the potential to provide exponential speedup for certain ML tasks, where quantum states can represent data and quantum gates can manipulate these states. However, it faces the challenge of the current non-fault tolerant era where, in practice, dealing with noise and the limited capacity of quantum chips is an active area of research. On the other hand, TNs are versatile mathematical tools for handling high-dimensional data in quantum physics and ML. They efficiently break down complex systems into manageable components, finding applications in quantum information theory, condensed matter physics, and deep learning, providing researchers with enhanced computational efficiency.

In this paper we want to concretely connect these two sides of quantum computing, exploiting one or the other in the various stages of construction of the overall algorithm. While some literature explored the comparison of these two approaches, only a few examples focus on the proposed idea of combining these two techniques. Indeed,

in the context of variational quantum algorithms, in [1, 2] the authors explored the use of Parametrized Quantum Circuits (PQCs) for calculating diverse properties of complex many-body systems, describing the benefits of this method relative to the use of TNs. While in [3], the paper describes a joint optimization framework utilizing both TNs and PQCs, the benefits of this style of joint training are predicted to give improved performance in QML, eventually numerically verified in [4].

Finally, [5] proposed a synergistic pretraining of quantum circuits via TNs applicable to a diverse range of circuit architectures and learning tasks, which was predicted to yield benefits in performance and trainability within general ML tasks.

In our work, we use TNs to prepare the initial state to be classified by a PQC. Specifically, we focus on the phase diagram reconstruction for the ANNNI model.

The ANNNI model [6–9] with transverse field consists of ferromagnetic interactions, $J_1 > 0$, between nearest neighbors and antiferromagnetic interactions, $J_2 < 0$, between next-nearest neighbors, competing with each other. The Hamiltonian is written as

$$H_{ANNNI} = -J_1 \sum_{i=1}^{N-1} \sigma_i^x \sigma_{i+1}^x - J_2 \sum_{i=1}^{N-2} \sigma_i^x \sigma_{i+2}^x - B \sum_{i=1}^N \sigma_i^z, \quad (1)$$

which we can rewrite in terms of the adimensional ratios $\kappa = -J_2/J_1$ and $h = B/J_1$. The former is called the *frustration parameter*.

This is the simplest model combining the effect of quantum fluctuations (owing to the presence of a trans-

* maria.cea@mpq.mpg.de

† michele.grossi@cern.ch

‡ saverio.monaco@desy.de

§ enrique.rico.ortega@gmail.com

¶ luca.tagliacozzo@iff.csic.es

** sofia.vallecorsa@cern.ch

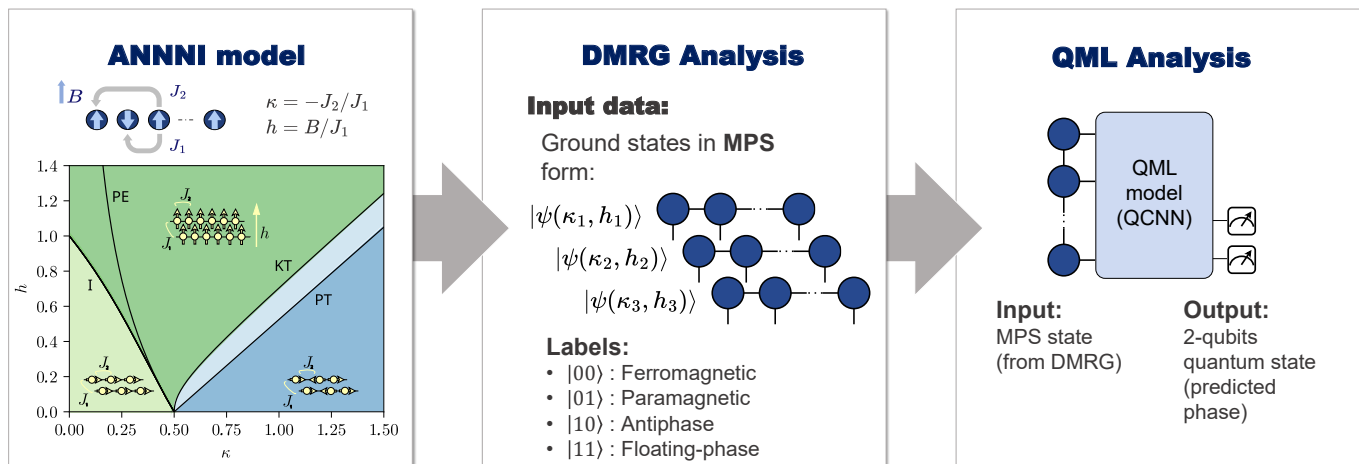


FIG. 1: Summary of the workflow: the left panel illustrates the graphical representation of the one-dimensional ANNNI model (Eq. 1) and its phase diagram. For the middle panel, we stress the use of TN as a tool to get the phase diagram of the model applying finite-size scaling analysis and as a source of the quantum state for the next level. The right panel showcases the QML analysis, with input data sourced from the DMRG, to classify different phases of the model.

verse magnetic field), and frustrated exchange interactions. As a consequence, it is a paradigm for the study of competition between magnetic ordering, frustration, and disordering effects. Competition can introduce dramatic effects in spin systems [10], leading to the appearance of a rich phase diagram.

Despite seeming too simple to describe realistic materials, this model may reproduce important features observed experimentally in systems that can be described by discrete models with effectively short-range competing interactions [8]. Some of these experimental findings include Lifshitz points, adsorbates, ferroelectrics, magnetic systems, alloys or polytypes. On the other side, the so-called floating phase emerging in the model is appealing to experimental researchers to explore it. This critical incommensurate phase has been observed very recently by using Rydberg-atom ladder arrays [11].

Several works have already studied the structure of the phase diagram of this model. Some of them treat the 2D classical model [7, 12–20] and others tackle the 1D quantum model [16, 19, 21–29]. Of the latter, some deal with finite systems and other with infinite systems [30]. However, in intermediate frustration and finite-transverse field regimes, the statements about phases and phase transitions are quite different. Two phases, paramagnetic and floating phase, have been addressed [19, 23, 30] and the former has been further divided into unmodulated and modulated one in some works [21, 22, 26, 28, 31]. However, the floating phase generates controversy in the literature since it was even not found in some of the previous studies [18, 24, 32, 33].

Building upon recent literature [34], we extend the analysis of the ANNNI model through QML techniques to larger spin models than previously studied, moving from a maximum of 12 spins to 20. The primary objec-

tives involve investigating how an increase in the number of qubits brings enhancements in overall accuracy and in the claimed generalization capabilities [35]. Additionally, our exploration of the generalization properties aims to comprehend how these models might extend to phase states not represented in the dataset, akin to the approach in [29].

Furthermore, we subject the ANNNI model to an in-depth TN analysis, bringing the finite-size analysis to models far larger than any currently reachable through fully quantum means, reaching up to 480 sites.

The paper is structured as follows: Section II delineates the applied methodologies derived from both TNs and QML. Section III showcases the numerical results obtained through the TN analysis providing some insights about the different phases emerging in the model and the phase transitions delimiting them. Section IV delves into the examination of the phase diagram, employing both supervised and unsupervised approaches by simulating Quantum Circuits. The structure of both analyses is highlighted in Figure 1. The paper concludes with a discussion of the results and potential future work in Section V.

II. METHODS

A. Tensor Networks

TNs [36–47] serve as versatile mathematical constructs designed for the representation and manipulation of high-dimensional data, particularly in the realms of quantum physics and ML [48–50]. TNs provide a generalization of the original ideas beyond the density matrix renormalization group (DMRG) [51–57] which as today

stands as the best algorithm to simulate one-dimensional quantum-many body systems. A generic TNs is built to provide an efficient encoding and manipulation of large data structures, by appropriately compressing them into small chunks according to specific patterns of correlations. Such small chunks become the individual tensors in the network. TNs have witnessed widespread applications across diverse fields, including quantum information theory, condensed matter physics at and out of equilibrium, and deep learning [58–60].

Matrix Product States (MPSs) [61–63] are the relevant TNs for DMRG and represent a particular class of TNs predominantly used for depicting quantum states in one-dimensional systems. Within the MPS framework, a quantum state is built as a product of matrices, each corresponding to a specific site within the system. The entanglement structure of the state is succinctly encapsulated through these matrices, providing a concise representation of many-body quantum states. Proving itself as a potent tool, MPSs have been instrumental in monitoring the properties of one-dimensional quantum systems [64, 65], involving aspects like ground state properties and dynamic behaviors.

In the context of MPSs, DMRG [51–57] becomes an iterative numerical algorithm that allows obtaining the best MPS for encoding the ground state of quantum systems in one and two dimensions [66–71].

Originally formulated for gapped Hamiltonians, DMRG can also be used to describe critical systems by leveraging on an appropriate finite-size scaling procedure [72–76] or by directly working in the thermodynamic limit [77–79]. Beyond its origins in condensed matter physics, it has evolved into a standard tool, finding applications in diverse domains, including quantum chemistry, high-energy physics, and ML.

As a result, DMRG has emerged as the *de facto* standard for analyzing phase diagrams of one-dimensional systems. Here, to make contact with QML results we characterize the phase diagram on a finite chain, and thus make use of finite-size scaling (FSS) techniques [80–82] which allows us to make predictions about the thermodynamic limit by studying local order parameters of finite systems. In addition to this, some insights on one-dimensional quantum field theory [83] are necessary to understand some of the phases and their limits. Numerical simulations have been carried out with TeNPy’s two-site DMRG [84].

B. Quantum Machine Learning

QML is an interdisciplinary field that merges the principles of quantum mechanics with the computational paradigms of ML. The intersection of quantum physics and ML has led to the development of algorithms and models designed to harness the unique properties of quantum systems to solve complex computational problems more efficiently than classical counterparts [85].

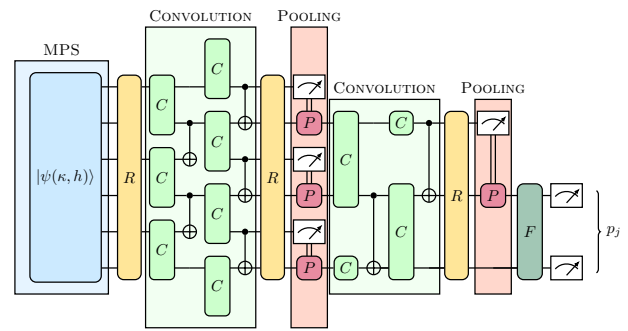


FIG. 2: Architecture of the QCNN: Input state preparation (blue), then alternating Convolution layers (green) and Pooling layers (red) and a Fully Connected layer (dark green) at the end [34]

QML algorithms often aim to outperform classical algorithms on specific tasks, capitalizing on the inherent advantages provided by quantum mechanics. Examples include quantum support vector machines, quantum clustering algorithms, and quantum neural networks. Researchers in this field are actively exploring the capabilities and limitations of quantum computers for ML applications. As quantum computing hardware continues to advance, and as more quantum devices become accessible, the field of quantum ML holds promise for revolutionizing the way we approach complex computational challenges. However, it also presents unique challenges, including issues related to qubit coherence, error correction, and the development of scalable quantum processors. In this work we focus mainly on algorithms that can, to some extent, be executed on current noisy quantum processors, leaving the discussion of *quantum linear-algebra based methods* to speed up an otherwise computationally costly training method in the context of large-scale fault-tolerant quantum computers.

Indeed, the design of genuinely quantum methods may yet offer advantages based on the idea of PQC (PQC-based methods) as the key building block of the model more generally, so-called quantum neural network models. It is important to note that learning separations (so, provable exponential advantages) for learning using quantum models have already been proven in most learning settings [86], subject to standard assumptions in complexity theory, and it can be shown [87] that these separations may be much more common when data is generated by a quantum process (under slightly stronger computational assumptions).

A fundamental limitation to the scaling up of most PQC-based ML methods is the so-called barren plateau phenomenon, where the gradients [88] of the cost function vanishes exponentially with the number of qubits employed. On such barren plateau landscapes, the cost function sharply concentrates on its mean, leading to an exponentially narrow minimum and typically requiring an exponential number of shots. While this phenomenon was originally identified in the context of variational

quantum algorithms and quantum neural networks, it has recently been shown that exponential concentration is also a barrier to the scalability of quantum generative modeling [89].

Quantum cost landscapes for a large class of problems can exhibit highly complex and non-convex landscapes that are resource intensive to optimize [90]. Recently, in [91] the authors provide a perspective article about the capabilities of PQC for barren plateau-free landscapes and connect them also to is classically simulable. This represents an important bridge between the connection we are making in this work, assigning different tasks to a quantum algorithm and a classical quantum-inspired one.

In the context of QML models for detecting phases in spin systems, two models stand out. The first, the QCNN, is a supervised learning model where the labels represent the different phases. The second, known as Quantum Anomaly Detection (AD), follows an unsupervised approach.

1. Quantum Convolutional Neural Network

QCNNs are a category of quantum circuits inspired by the widely popular classical counterpart, Convolutional Neural Networks (CNNs). These quantum architectures, much like CNNs, aim to learn representations from input data by exploiting their inherent local properties. Indeed, the model was originally proposed in [92] for the task of detecting phase transitions, where these local properties equate to the interactions between the neighboring spins

Figure 2 provides a visualization of the employed QCNN, composed of three primary components:

- Convolution layers: these involve the application of alternating unitaries to pairs of neighboring spins.
- Pooling layers: half of the qubits are measured, and depending on the result of the measurement, a different rotation is applied to the remaining qubits.
- Fully connected layer: following alternating convolution and pooling layers, a final unitary is applied to the remaining qubits.

This architecture is an excellent choice for a supervised approach to learning the phase of spin models. Its strength lies not only in its ability to utilize local properties of the input data but also in its proven remarkable training capabilities compared to other PQCs. This advantage stems from its unique structure, which includes a local final measurement [93] and a total number of parametrized gates that scale logarithmically with the number of qubits. These two properties contribute to a resulting suppression of Barren Plateaus [94].

Furthermore, recent advancements have significantly optimized the effective implementation of such architecture on real hardware [95, 96].

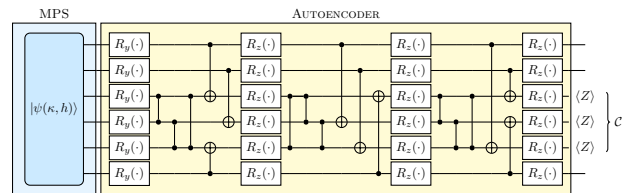


FIG. 3: Architecture of the Anomaly detection circuit (yellow) and input state preparation (blue). An example architecture for 6 qubits, with half designated *trash* qubits positioned at the center. [34]

2. Quantum Anomaly Detection

Quantum AD is another architecture inspired by deep learning models. This architecture functions as the quantum equivalent of an Autoencoder. Due to the inversion property of quantum circuits, only the forward encoding part is considered and trained. The training process involves minimizing the Pauli-Z expectation values of a subset of the qubits, known as *trash qubits*. The objective is for the model to learn an effective unitary operation capable of compressing all the information in the remaining un-measured qubits:

$$\mathcal{U}(\vec{\theta})|\psi\rangle^N = |0\rangle^{\otimes K} \otimes |\phi\rangle^{N-K} \quad (2)$$

where N is the total number of qubits, and K is the number of trash qubits.

Figure 3 shows an example of a 6-qubit AD ($N = 6$) with 3 trash qubits ($K = 3$).

III. TENSOR NETWORK ANALYSIS

Before moving on to the hybrid TN/QML approach we first show that TNs fully captures interesting features in the phase diagram of the ANNNI model, giving results in good agreement with other state-of-the-art approaches.

From earlier studies including simulations of both finite [26] and infinite [30, 97] systems and the study of a spin chain that can be mapped onto our model using a non-local transformation [97, 98], we expect a phase diagram like the one in Fig. 4, with four different phases (the ferromagnetic phase, the paramagnetic phase, the floating phase and the antiphase) and a disordered line [13]. All phases are gapped except the gapless floating phase. A system is known to be gapless if there are excitations at arbitrarily low energies in the infinite lattice limit (and gapped if not) [99]. In this work, as we simulate finite systems, there is necessarily a nonzero energy separating the ground state and the first excited state. However, this energy spacing can either remain finite or approach zero in the thermodynamic limit.

To observe the transitions and the properties of the different phases, we fix the value of the transverse field, h , and vary the frustration parameter, κ . When the system

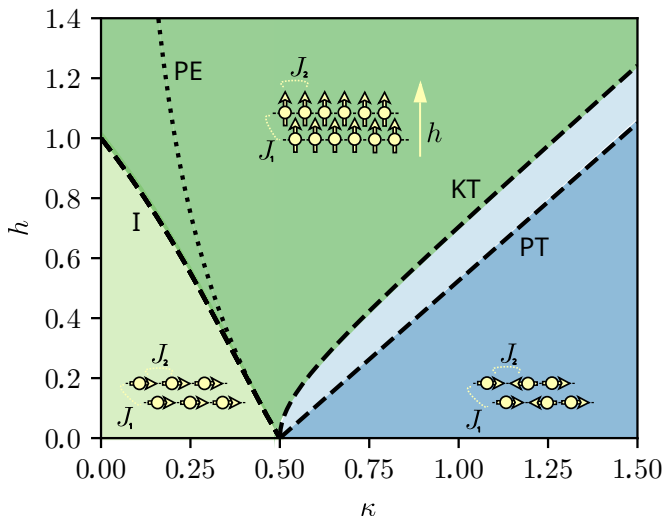


FIG. 4: Phase diagram of the quantum one-dimensional ANNNI model of Eq. 1. The dotted line is the exactly-solvable Peschel-Emery (PE) line $h = 1/4\kappa - \kappa$ [13]. Dashed lines represent Ising (I), Kosterlitz-Thouless (KT), and Pokrovsky-Talapov (PT) phase transitions. The spin chain can be seen as a ladder of two spin chains as sketched in the cartoon spin configurations.

goes through a phase transition (i.e., at a critical point), a qualitative change in correlations of the ground state occurs. A measure of the range over which these correlations approach zero is called the correlation length, ξ . In gapped phases, ξ is finite and the correlation functions of local operators typically exhibit exponential decay with distance,

$$C_{i,j}^{zz} = \langle \sigma_i^z \sigma_j^z \rangle - \langle \sigma_i^z \rangle \langle \sigma_j^z \rangle \propto e^{-|i-j|/\xi}. \quad (3)$$

In gapless phases, this quantity can become infinite and the correlation functions follow a power-law behavior with distance.

$$C_{i,j}^{zz} \propto \frac{1}{|i-j|^\eta}. \quad (4)$$

When the system is approaching a critical point, the correlation length diverges and how it does so allows us to know the nature of the transition. Notice that correlation length extracted from different operators could have different values but they are all proportional and scale in the same way with the system size.

In Fig. 5, the inverse of the correlation length along the horizontal cut at $h = 0.5$ is shown, providing qualitative insights into the nature of the phase transitions. At low values of frustration, the inverse of the correlation length vanishes linearly in agreement with the Ising (I) critical exponent $\nu = 1$. After this, it reaches its maximum at a sharp kink that corresponds to the disorder point [13, 15]. Beyond this point, it decreases quickly, in agreement with the exponential divergence of the correlation length typical for a Kosterlitz-Thouless (KT) transition [100]. Approaching the phase transition between the critical phase

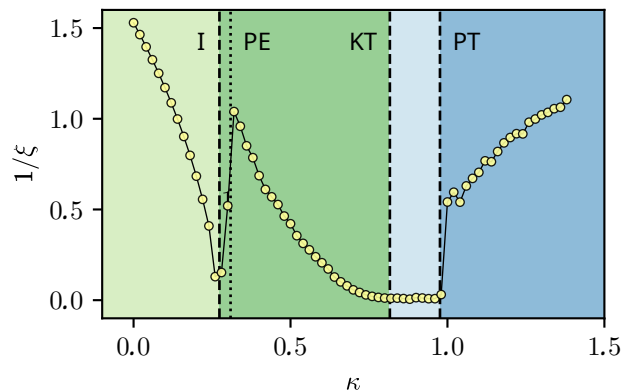


FIG. 5: Inverse of the correlation length computed from $C_{i,j}^{zz}$ as a function of κ along the horizontal cut at $h = 0.5$ obtained on a finite-size system with $N = 240$ sites with open boundary conditions. Colors indicate different phases: the ferromagnetic phase (light green), the paramagnetic phase (dark green), the floating phase (light blue), and the antiphase (dark blue) from left to right. Phase transitions according to previous results [13, 26, 102] are also shown by dashed lines: Ising (I) transition, Kosterlitz-Thouless (KT) transition, and Pokrovsky-Talapov (PT) transition. The dotted line is the exactly solvable Peschel-Emery (PE) line [13].

and the antiphase from the latter, the inverse of the correlation length vanishes with a critical exponent smaller than one, in agreement with the Pokrovsky-Talapov (PT) critical exponent $\nu = 1/2$ [101]. Details can be found in Appendix A.

A. Ferromagnetic Phase and Paramagnetic Phase

We now examine more closely the phase transition between the ferromagnetic and paramagnetic phases.

In the ferromagnetic phase, the next neighbor interactions dominate and all the spins are aligned in the x direction, $|\rightarrow\rightarrow\cdots\rangle$ or $|\leftarrow\leftarrow\cdots\rangle$ (note that $\sigma_j^x |\rightleftharpoons\rangle = \pm |\rightleftharpoons\rangle$), leading to a uniform magnetization. In the paramagnetic phase, the transverse magnetic field dominates and makes the spins be aligned in the z direction, $|\uparrow\uparrow\cdots\rangle$ (note that $\sigma_j^z |\uparrow\rangle = |\uparrow\rangle$). As a result, the magnetization along the x direction is a relevant order parameter to characterize the quantum phase transition,

$$M^x = \frac{1}{N} \sum_{j=1}^N \sigma_j^x. \quad (5)$$

At low values of frustration, the magnetization is expected to be non-zero, indicating an ordered phase. As the frustration increases, there is a critical value where the magnetization undergoes a sudden change, signaling a quantum phase transition to a disordered phase with the magnetization approaching zero. Although the magnetization of an infinite system shows a discontinuity, this

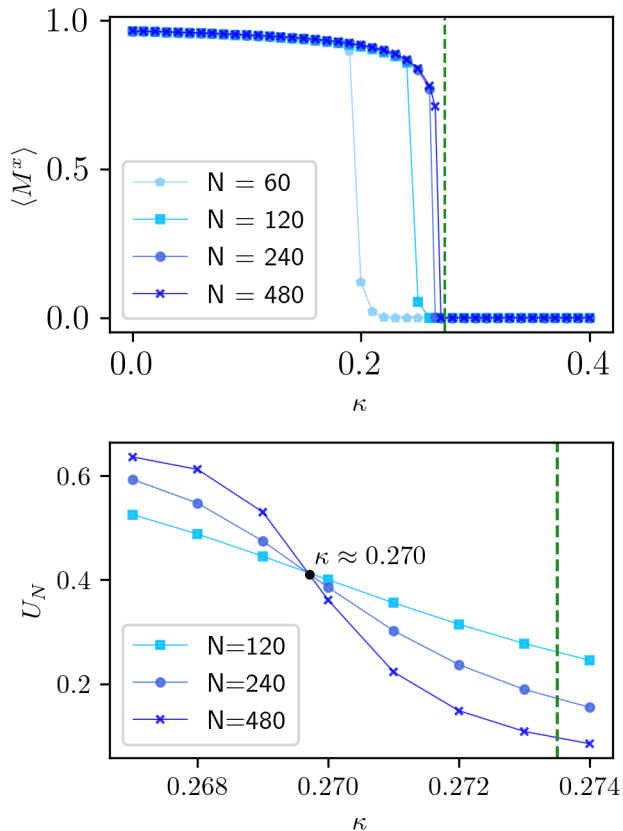


FIG. 6: (Up) Magnetization along x (see Eq. 5) obtained on four finite-size systems ($N = 60, 120, 240, 480$) with open boundary conditions along the horizontal cut at $h = 0.5$. As expected, magnetization in the ferromagnetic phase is non-zero and in the paramagnetic phase is zero. Note that the phase transition approaches the perturbative analysis prediction as the length of the chain increases. (Down) Binder's cumulant (see Eq. 6) for κ -values in the surroundings of the critical point extracted from Eq. 7.

abrupt step is rounded when the system size N is finite [80]. Consequently, the critical frustration value at which the phase transition occurs may shift slightly for finite systems compared to the thermodynamic limit. To make predictions of this limit by working with finite systems, we make use of Finite-Size Scaling (FSS) [80, 81]. Within this framework, Binder's cumulant can be used to locate the precise transition point [82]

$$U_N = 1 - \frac{\langle (M^x)^4 \rangle_N}{3 \langle (M^x)^2 \rangle_N^2}. \quad (6)$$

Since this ratio is built to be size-independent at the critical point, by plotting it as a function of the parameter of the model for different system sizes, one can identify the critical point as the crossing of the lines.

The phase boundary between the ferromagnetic and

the paramagnetic phases can be obtained by using perturbation theory for $\kappa < 0.5$, splitting the Hamiltonian in a classical Ising part and a small transverse fluctuation, an approximate expression for the critical line is obtained in [9] and reads

$$h_I \approx \frac{1 - \kappa}{\kappa} \left(1 - \sqrt{\frac{1 - 3\kappa + 4\kappa^2}{1 - \kappa}} \right), \quad (7)$$

and corresponds to an Ising-like transition [102].

Fig. 6 (upper panel) shows the behavior of the local order parameter $\langle M^x \rangle$, which allows us to differentiate both the ferromagnetic and the paramagnetic phases. Finite-size effects appear and it can be seen how the discontinuity in magnetization approaches the critical point and becomes steeper as the system size increases. By computing Binder's cumulant through Eq. 6, we get $\kappa_I = 0.270$, see Fig. 6 (lower panel).

B. Floating Phase

1. Luttinger Liquid and Friedel Oscillations

In 1D quantum physics, the floating phase [101, 103, 104] is described by a Luttinger liquid with algebraic incommensurate correlations [83]. Its properties are described by a bosonic conformal field theory and the decay of all the correlation functions is controlled by the parameter K , often referred to as the Luttinger liquid parameter [83, 105]. This Luttinger liquid phase is stable against superconducting perturbations and spontaneous translation symmetry breaking due to an emergent $U(1)$ symmetry when the Luttinger exponent lies within the interval $1/4 < K < 1/2$ [97]. Furthermore, open boundary conditions act as an impurity and lead to Friedel oscillations in spin density. According to Boundary Conformal Field Theory (BCFT), the profile takes the following form [106–108]:

$$\langle \widetilde{\sigma}_j^z \rangle \propto \frac{\cos(qj + \alpha)}{[(N/\pi) \sin(\pi j/N)]^K}, \quad (8)$$

where K is the Luttinger exponent, q is the incommensurate wave-vector and α is a phase shift. By fitting Friedel oscillations we can get an accurate estimate of both the Luttinger parameter K and the incommensurate wave-vector q [109]. One example of such fits is shown in Fig. 7, where the uniform part of the spin-density, $\langle \sigma_j^z \rangle$, has been subtracted. Details can be found in Appendix B.

2. Kosterlitz-Thouless transition

A Kosterlitz-Thouless (KT) transition appears between the paramagnetic phase and the floating phase.

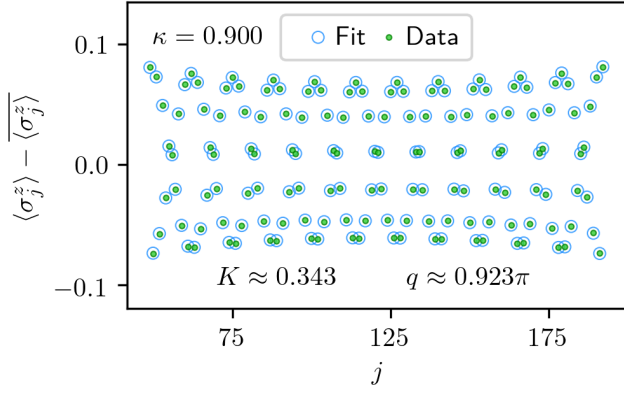


FIG. 7: Friedel oscillation pattern inside the floating phase for $h = 0.5$ and $\kappa = 0.900$ obtained on a finite-size system of $N = 240$ sites with open boundary conditions. Green points are DMRG data and blue circles are the result of the fit with Eq. 8 (note the very accurate agreement). The uniform part of the spin-density $\langle \sigma_j^z \rangle$ has been subtracted (see Appendix B).

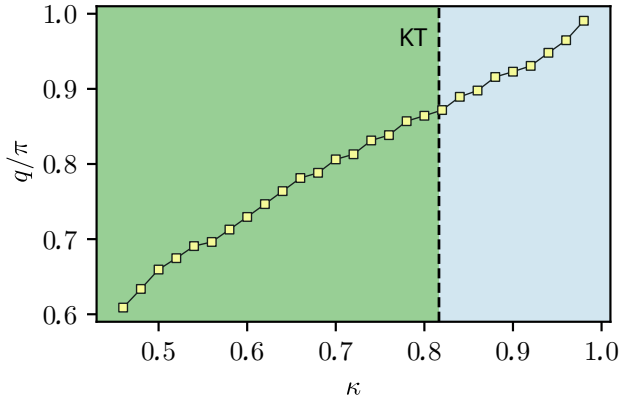


FIG. 8: Incommensurate wave-vector q obtained on a finite-size system with $N = 240$ sites with open boundary conditions along the horizontal cut at $h = 0.5$. As it is shown, incommensurability doesn't vanish in the paramagnetic phase. Therefore, the Kosterlitz-Thouless (KT) transition is an incommensurate-incommensurate phase transition.

In this model, it is an incommensurate-incommensurate transition, as we see in Fig. 8. As mentioned in [97, 98], the critical point is associated with the Luttinger liquid exponent taking the value $K = 1/2$. Then, we can locate the transition by extracting the Luttinger liquid exponent and finding the value corresponding to $K = 1/2$.

Numerical simulations involving different techniques suggest that the KT critical line is given by [26]

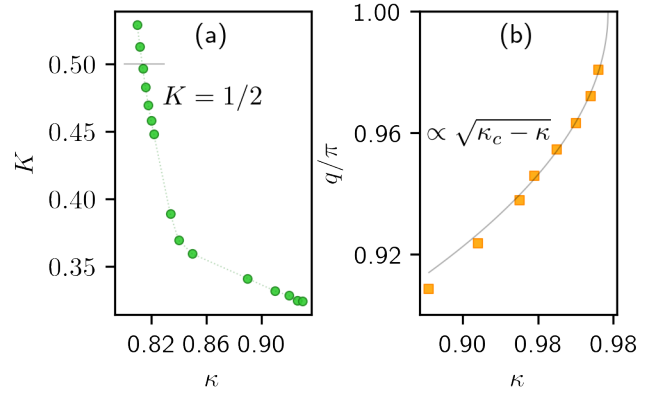


FIG. 9: (a) Luttinger liquid exponent K and (b) incommensurate wave-vector q obtained on a finite-size system with $N = 240$ sites with open boundary conditions along the horizontal cut at $h = 0.5$. The Kosterlitz-Thouless (KT) transition appears when $K = 1/2$ and the Pokrovsky-Talapov (PT) transition arises when incommensurability vanishes. The solid line in (b) is a fit assuming the Pokrovsky-Talapov (PT) critical exponent $\nu = 1/2$.

$$h_{KT}(\kappa) \cong 1.05 \sqrt{\left(\kappa - \frac{1}{2}\right) (\kappa - 0.1)}. \quad (9)$$

Fig. 9(a) shows the K exponent in terms of frustration. The value we get for the critical point is $\kappa_{KT} = 0.814$. This means that our result presents a relative error of 0.36% concerning previous calculations.

3. Pokrovsky-Talapov transition

The transition between the floating phase and the antiphase (discussed below) is a commensurate-incommensurate transition expected to be in the Pokrovsky-Talapov (PT) [101, 110] universality class. Then, we can fit the incommensurate wave-vector q as $q/\pi \propto (\kappa_{PT} - \kappa)^\nu$, where ν takes the value of $\nu = 1/2$ at the PT transition. Close to the critical point a square root-like behavior arises and we can extract a numerical value for the critical point with high accuracy. We obtain $\kappa_{PT} = 0.977$ with a root mean squared error of $\approx 10^{-3}$.

Also from [26], we have an expression for this critical line given by

$$h_{PT}(\kappa) \cong 1.05 \left(\kappa - \frac{1}{2}\right), \quad (10)$$

from which we estimate a relative error of 0.10%.

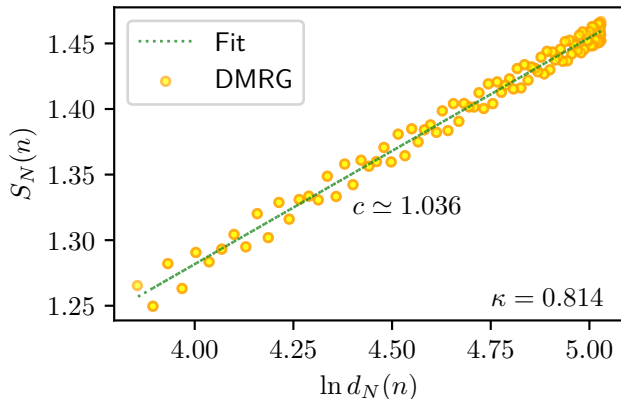


FIG. 10: Entanglement entropy with conformal distance $d_N(n)$ at $h = 0.5$ and $\kappa = 0.814$ for a finite-size system with $N = 240$ sites for open boundary conditions. The obtained value for the central charge in the critical point agrees within 3.6% with the CFT prediction $c = 1$ for a Luttinger liquid.

4. Entanglement entropy

According to Conformal Field Theory (CFT), the entanglement entropy at critical points in a finite-size chain with open boundary conditions scales with the block size n as [73, 74, 76, 111, 112]

$$S_N(n) = \frac{c}{6} \ln d_N(n) + s_1 + \ln g, \quad (11)$$

where $d_N(n) = \frac{2N}{\pi} \sin(\frac{\pi n}{N})$ is the conformal distance, and s_1 and $\ln g$ are non-universal constants.

We use Eq. 11 to extract the central charge numerically. Close to the KT critical line, the central charge can be extracted with sufficient accuracy even from relatively small chains, see Fig. 10 [113].

The obtained value for the central charge in the critical point agrees within 3.6% for $N = 240$ with the CFT prediction $c = 1$ for a Luttinger liquid. This value of the central charge could be understood if we see the model as two quantum Ising chains coupled by a “zig-zag” interaction with strength J_1 [16]. Inside the floating phase and in the large κ limit, the model is conformally invariant with central charge $c = 1/2 + 1/2 = 1$, i.e. two critical Ising models.

C. Antiphase

In the antiphase, the antiferromagnetic next-nearest neighbor interactions dominate and the ground state is $|\rightarrow\leftarrow\rightarrow\leftarrow\dots\rangle$ or $|\leftarrow\leftarrow\rightarrow\rightarrow\dots\rangle$. From the relative position of spins, it is easy to see that a convenient local order parameter to identify this phase is the so-called “staggered magnetization”, defined as

$$S^x = \frac{1}{N} (\sigma_1^x + \sigma_2^x - \sigma_3^x - \sigma_4^x + \dots). \quad (12)$$

However, the critical points extracted from the finite-size scaling analysis are not as accurate as the ones extracted from the incommensurate wave vector vanishing in the PT transition.

IV. QUANTUM MACHINE LEARNING ANALYSIS

A. States preparation

Both QML architectures aforementioned use the ground states of the Hamiltonian of the ANNNI model (Eq. 1) at different values of κ and h as inputs. A standard approach to access and load the states into the quantum circuits is to use the technique called Variational Quantum Eigensolver (VQE). Through VQE, it is possible to find a set of parameters $\vec{\theta}^*$ for a given Ansatz U such that the output state of the circuit $U(\vec{\theta}^*)|0\rangle^{\otimes N}$ is close to the sought ground-state wavefunction [114]. This is accomplished by using the Rayleigh-Ritz variational principle, by minimizing the energy expectation value of the parametrized output wavefunction:

$$\operatorname{argmin}_{\vec{\theta}} \frac{\langle \psi(\vec{\theta}) | \mathcal{H} | \psi(\vec{\theta}) \rangle}{\langle \psi(\vec{\theta}) | \psi(\vec{\theta}) \rangle} \quad (13)$$

where

$$|\psi(\vec{\theta})\rangle := U(\vec{\theta})|0\rangle^{\otimes N}$$

During training, the output of the circuit is expected to converge toward the state with the lowest achievable energy, thus the ground state.

However, for this analysis, it has been considered more convenient to avoid using the VQE technique altogether due to the need for training for each combination of κ and h at each studied system size. Moreover, training VQE on a simulator becomes inefficient as both simulation times and the number of shots required exponentially increase with a high number N of qubits. The decision instead has been made to employ the MPS states acquired from the DMRG analysis as inputs. These states are integrated into the circuit through the PennyLane function `qml.QubitStateVector`, allowing the overwrite of the initial state ($|0\rangle^{\otimes N}$) with any desired state.

This approach, however, is possible only in simulator-based analyses, where full access to wavefunctions is available. On real hardware, such an operation is unfeasible. Moreover, this approach is limited by the computation of the full state vector. An alternative approach would require transposing the MPS directly into a PQC [115], which might eventually facilitate the implementation of this analysis on real quantum hardware.

B. QCNN

QCNNs offer a supervised approach for detecting the phase transitions of the ANNNI model. Like any supervised approach, the core objective is to build a model where the predictions closely match their corresponding labels.

In this scenario, the labels are encoded in a 2-qubit quantum state:

- Ferromagnetic : $|00\rangle$
- Paramagnetic : $|01\rangle$
- Antiphase : $|10\rangle$
- Floating phase : $|11\rangle$

The training procedure consists of the minimization of the following cross-entropy loss function:

$$\mathcal{L} = -\frac{1}{|\mathcal{M}|} \sum_{(\kappa, h) \in \mathcal{M}} \sum_{j=1}^K y_j(\kappa, h) \log(p_j(\kappa, h)), \quad (14)$$

where \mathcal{M} is the set of parameters of the training set, $y_i(\kappa, h)$ is the probability vector of the label of the corresponding ground state of $\mathcal{H}(\kappa, h)$, and $p_i(\kappa, h)$ is the probability vector of the output state of the QCNN.

Two distinct analyses were conducted, each employing different regions in the phase diagram as the training set. The first analysis mirrors the approach outlined in [34], utilizing exclusively the points within the *integrable* part of the phase diagram $\{(\kappa, h) \in \{0\} \times [0, 2]\} \cup \{(\kappa, h) \in [0, 1] \times \{0\}\}$, specifically, the points lying on the two axes, $\kappa = 0$ (representing the simple transverse field case) and $h = 0$ (representing the quasi-classical model). This choice allows for the analytical derivation of labels, however, it omits any points associated with the floating phase case, as none are present on the two axes, thus making the classifier entirely agnostic regarding the fourth phase.

For the second analysis, the training set includes the entire phase diagram within the ranges of h and κ , and the labels are derived from the DMRG analysis. This second analysis is not made to showcase the proficiency of the QCNN in a conventional setting. The main goal is to evaluate how the finite system size considered affects the indistinguishability of the points of this particular phase.

Both analyses were carried out using different values for the number of spins N specifically, 12, 16, and 20. Given the considerable size of the circuits simulated, the training was structured with the primary goal of loading the minimal amount of state vectors into memory simultaneously.

At the start of training, a limited number s of input state vectors are drawn randomly from each class. After each set number of epochs e , new input vectors are randomly drawn, and the training process continues. In this setup, the total number of input state vectors loaded at

any given time is given by $s \times K$ where s is significantly smaller than the total number of training inputs, and K represents the number of classes present in the training set. The selection of s was determined based on the size of each state vector, as defined by N , ensuring that the highest number of inputs could be processed without exceeding memory constraints.

1. Analytical points only

In the first analysis, the training set comprises solely the analytical points located on the axes. Following the training process, the model is subsequently employed across the entire phase diagram to predict the phase at each combination of κ and h , leveraging the high generalization capabilities highlighted in [35] for quantum models. Given the absence of floating phase points within the training set, the model tends to avoid predicting any points belonging to that particular class.

Figure 11 displays the QCNN predictions at N being 12 (left), 16 (middle), and 20 (right).

The comparison of the three images reveals two distinct patterns. Firstly, the accuracy of the transition between ferromagnetic and paramagnetic phases improves with an increase in the number of spins in the system. Instead, the predicted transition between the antiphase and paramagnetic phases shifts as the number of spins rises from the Kosterlitz-Thouless transition line to possibly plateauing on the Pokrovsky-Talapov line. The presence of the floating phase becomes increasingly evident with a higher number of spins, and this is speculated to be the main reason why the predicted transition line shifts as the system size increases with larger models tending to classify floating phase points as paramagnetic rather than anti-phase.

2. All classes

In the second analysis, every point, including those belonging to the floating phase, is integrated into the pool of training points randomly drawn. Figure 12 showcases the prediction outcomes of the QCNN for N being of 12, 16, and 20. As in the previous analysis, the accuracy of the transition line between ferromagnetic and paramagnetic phases increases with the system's size. However, at every system size, all models faced difficulties in precisely defining the region of the floating phase. This suggests that a system with only 20 spins still experiences significant limitations due to its constrained size. It is reasonable to assume that this analysis would improve in accuracy with a higher number of spins.

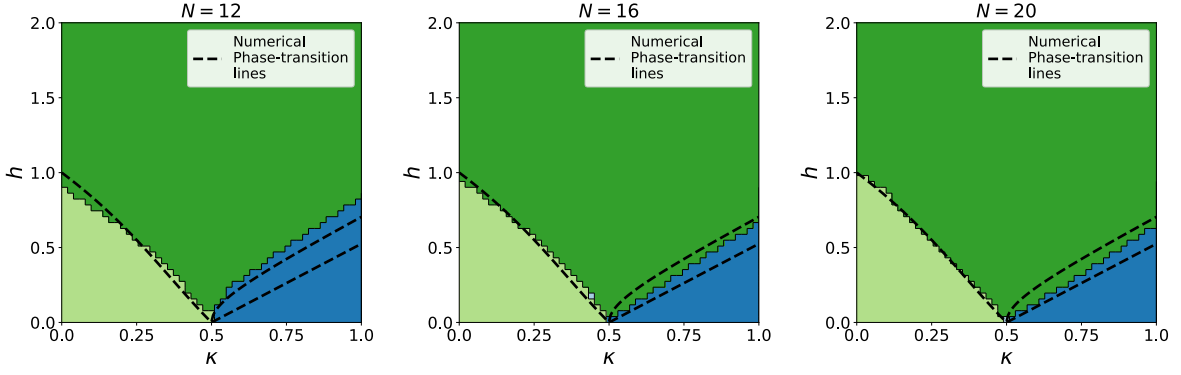


FIG. 11: Predictions of the QCNNS trained on the analytical points of the ANNNI Spin Model at different system sizes: $N = 12$ (left), $N = 16$ (middle), and $N = 20$ (right). Colors represent Ferromagnetic (light green), Paramagnetic (dark green), Antiphase (dark blue), and Floating Phase (light blue) as a function of the external magnetic field ($h = B/J_1$) and interaction strength ratio ($\kappa = -J_2/J_1$) (refer to eq. 1).

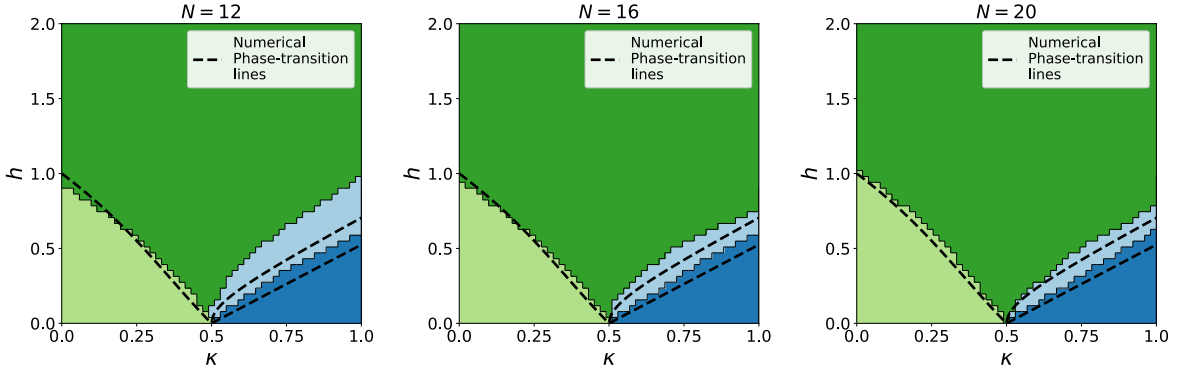


FIG. 12: Predictions of the QCNNS, trained on a subset of points from each phase of the ANNNI model at various system sizes: $N = 12$ (left), $N = 16$ (middle), and $N = 20$ (right). The color scheme indicates Ferromagnetic (light green), Paramagnetic (dark green), Antiphase (dark blue), and Floating Phase (light blue), as a function of the external magnetic field ($h = B/J_1$) and interaction strength ratio ($\kappa = -J_2/J_1$) (refer to eq. 1).

C. Anomaly Detection

An alternative approach to discovering the phase landscape of a spin system consists of employing the AD architecture. By operating in an unsupervised manner, it effectively bypasses the bottleneck of acquiring training labels inherent in such a model. For this main reason, the AD architecture stands as a suitable choice for identifying phases beyond the analytical ranges, such as the Floating phase.

The training process for this architecture is as follows: a single state is selected as the training event, and the training is carried out to achieve the compression outlined in equation 2. This involves the minimization of the following loss function:

$$C = \frac{1}{2} \sum_{j \in q_T} (1 - \langle \sigma_j^z \rangle), \quad (15)$$

where q_T refers to the selected trash qubits, constituting

$N/2$ out of the total N .

After training, each other state of the phase diagram is compressed through anomaly detection, and the corresponding cost value is assigned.

Typically, states belonging to the same phase as the training event undergo optimal compression, given their inherent similarity. Conversely, states from other phases tend to exhibit higher values in the cost function. Notably, the compression shares values consistently across different phases, allowing for the outline of all existing phases in the spin model.

Contrary to the previous analysis [34], the anomaly detection has been applied to even larger spin models. The aim is to identify the floating phase in the phase diagram through this model, which may have been previously obscured by the constraints of the smaller system size.

Figure 13 depicts the compression scores generated by the anomaly detection for N equals 6, 12, and 18.

All anomaly detection models were trained to compress the point $(\kappa, h) = (0, 0)$ of the Hamiltonian, represent-

ing the case with no magnetic field and no next-nearest neighbor interaction between spins.

Two main observations can be drawn from the figure. Firstly the boundaries between different phases become increasingly sharp with larger system sizes. Secondly, up to 12 qubits (the maximum limit from the previous analysis), no floating phase can be discerned from the compression score. However, at $N = 18$, the presence of a fourth phase becomes evident, indicated by a dark blue shade in the area associated with the floating phase.

When $N = 18$, the system size is sufficiently large to identify the presence of the Floating Phase. However, it seems that the size is still limited for the detection of this phase, as the boundaries of the dark green shade appear imprecise and fuzzy.

V. SUMMARY AND DISCUSSION

In this work, we defined a QML pipeline, made by TN and QCNN to perform the classification of different phases of the ANNNI model. Starting from training data obtained with DMRG we input those wavefunctions in the QCNN. In this configuration, we benefit from the flexibility and scalability of TN together with the trainability guarantee and performance of QCNN.

The TN analysis provides us with numerical pieces of evidence of changes in the properties of the ground state, leading to the understanding of the phase diagram. By using the most recent techniques proposed in [98, 109, 113], we have identified the phase transitions appearing in the model by fixing the value of the transverse magnetic field. We have found agreement with previous DMRG results [26] and perturbative analysis [102]. Moreover, our results also coincide with those extracted from the model resulting from the Kramers-Wannier transformation of the ANNNI model, given by analyses with both finite [98] and infinite systems [97].

On the QCNN side, we confirmed the validity of the architecture in identifying the phase transitions of the ANNNI model, as previously demonstrated in [34]. Additionally, by increasing significantly the system size of the model from 12 to a maximum of 20 sites, we have been able to track the behavior of the classifier as the number of qubits N increases. As a supervised learning model, the QCNN lacks an out-of-the-box mechanism for training to recognize the floating phase, as no points within that phase belong to the analytical subspace of the phase diagram. A related study [29] successfully identified the Antiphase - Paramagnetic phase transition through a similar generalization approach employed in this analysis. This suggests that a comparable approach could be eventually implemented to the QCNN to detect the floating phase region by plain generalization.

An alternative approach, that has shown promising results, is the AD architecture first introduced in [116]. By employing the architecture on the ANNNI model at a

higher system size than ever before, here, it has been demonstrated that the AD can detect the floating phase in a fully unsupervised manner, furthermore, the scaling analysis presented suggest that by increasing even more the system size, the model will be able to accurately trace the floating phase.

One of the main features shared by both architectures is the use of the ground-state wavefunctions of the ANNNI model as inputs. This can be achieved by employing the VQE, as demonstrated previously in [34]. Alternatively, the ground-state wavefunctions can be obtained classically through the DMRG and then transposed into PQCs using techniques outlined in [115, 117]. These methods create a bridge between TNs and QML, enabling faster state preparation with greater accuracy[117]. In this work, we followed the latter approach, implementing the MPS wavefunctions as input obtained through DMRG in the TN analysis.

In summary, although TN analysis provides more accurate results as larger system sizes can be achieved, the amount of entanglement in the system could limit the study of more complex models. On the other hand, quantum computers promise to simulate states of high entanglement more effectively than classical ones. Therefore, despite not being at this point right now, classifying phase diagrams through QML techniques seems to be a promising avenue.

ACKNOWLEDGMENTS

M.C. acknowledges Natalia Chepiga for useful discussions regarding the nature of the KT transition and the effects of boundary conditions. M.C is partly funded by the Deutsche Forschungsgemeinschaft (DFG, German Research Foundation) under Germany’s Excellence Strategy –EXC-2111–390814868 and by Research Unit FOR 5522 (grant nr. 499180199).

M.G. and S.V. are supported by CERN through the CERN Quantum Technology Initiative.

E.R. is supported by the grant PID2021-126273NB-I00 funded by MCIN/AEI/ 10.13039/501100011033 and by “ERDF A way of making Europe” and the Basque Government through Grant No. IT1470-22.

L.T. acknowledges support from the Proyecto Sinérgico CAM 2020 Y2020/TCS-6545 (NanoQuCo-CM), the CSIC Research Platform on Quantum Technologies PTI-001, and from Spanish projects PID2021-127968NB-I00 and TED2021-130552B-C22 funded by MCIN/AEI/10.13039/501100011033/FEDER, UE and MCIN/AEI/10.13039/501100011033, respectively.

This work was supported by the EU via QuantERA project T-NISQ grant PCI2022-132984 funded by MCIN/AEI/10.13039/501100011033 and by the European Union “NextGenerationEU”/PRTR. This work has been financially supported by the Ministry of Economic Affairs and Digital Transformation of the Spanish Government through the QUANTUM ENIA project called

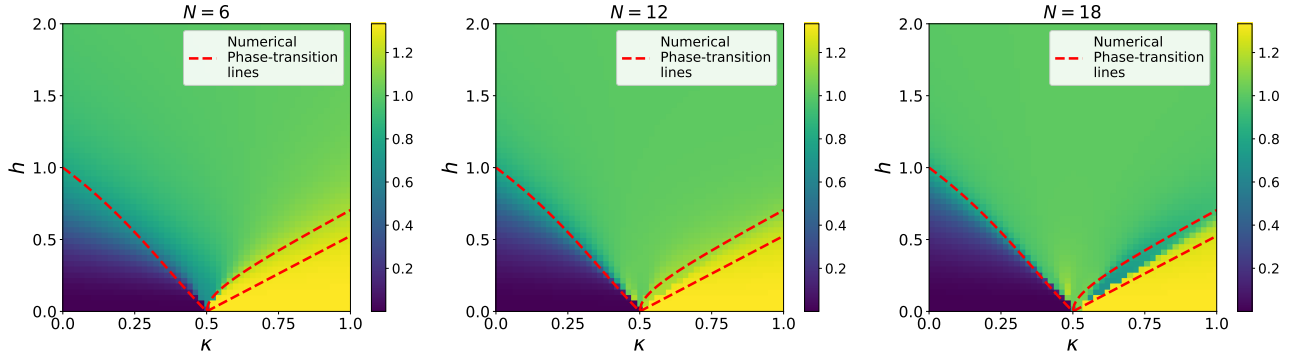


FIG. 13: Compression Scores \mathcal{C} of the AD circuits trained on the $(\kappa, h) = (0, 0)$ point of the ANNNI model phase diagram at different system sizes N : 6 (left), 12 (middle), and 18 (right). The scores are showcased as a function of the interaction strength ratio ($\kappa = -J_2/J_1$) and the external magnetic field ($h = B/J_1$). Lower compression scores indicate better disentanglement of trash qubits from others, as defined by eq. 2.

– Quantum Spin project, and by the European Union through the Recovery, Transformation, and Resilience Plan – NextGenerationEU within the framework of the Digital Spain 2026 Agenda.

Appendix A: Extraction of the Correlation Length

Despite the different behavior of the correlation length in gapped and gapless phases, since we work with finite systems (i.e., with finite bond dimensions), we do not expect its divergence at criticality. Therefore, we can extract the value of the correlation length, as proposed in [98, 109, 113], by considering the correlation function

$$C_{i,j}^{zz} = \langle \sigma_i^z \sigma_j^z \rangle - \langle \sigma_i^z \rangle \langle \sigma_j^z \rangle, \quad (\text{A1})$$

where i, j denote different sites. This function is related to the Ornstein-Zenicke form [118]:

$$C_{i,j}^{zz} \propto \frac{e^{-|i-j|/\xi}}{\sqrt{|i-j|}} \cos(q|i-j| + \phi_0), \quad (\text{A2})$$

where the correlation length ξ , the wave-vector q and the initial phase ϕ_0 are fitting parameters. One example of such fits is shown in Fig. 14. We discard the oscillations and fit the main slope of the decay as shown for high precision in the value obtained for ξ . Note that the fit is performed in a semi-log scale $\ln C^{zz}(x = |i-j|) \approx cte - x/\xi - \ln(x)/2$.

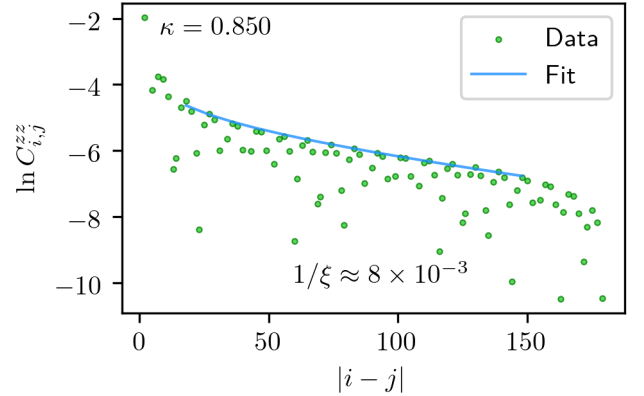


FIG. 14: Extraction of the correlation length ξ from correlations in the z direction. These transverse correlations are obtained for $h = 0.5$ inside the floating phase on a finite-size system with $N = 240$ and open boundary conditions. The green points are DMRG data and the blue line is the result of the fit with Eq. A2. Oscillations have been removed to fit the main slope of the decay. Note the semi-log scale.

Appendix B: Extraction of the Luttinger Liquid Parameters

To extract the Luttinger liquid exponent inside the floating phase, we have fitted the Friedel oscillations of the spin-density profile induced by the open boundary conditions with Eq. 8. Open ends in the chain break translational invariance and there is a slowly decaying alternating term in the spin-density

$$\langle \sigma_j^z \rangle = \overline{\langle \sigma_j^z \rangle} + (-1)^j \widetilde{\langle \sigma_j^z \rangle}, \quad (\text{B1})$$

where $\widetilde{\langle \sigma_j^z \rangle}$ becomes non-zero near the boundary and decays slowly away from it [119]. In order to obtain both

$\overline{\langle \sigma_j^z \rangle}$ and $\widetilde{\langle \sigma_j^z \rangle}$, we follow the 7-point formulas derived in [119]:

$$\begin{aligned} \overline{\langle \sigma_j^z \rangle} &= -\frac{15}{496}f(j-3) - \frac{1}{248}f(j-2) + \frac{71}{248}f(j-1) \\ &\quad + \frac{1}{2}f(j) + \frac{137}{496}f(j+1) + \frac{1}{248}f(j+2) - \frac{1}{31}f(j+3), \\ \widetilde{\langle \sigma_j^z \rangle} &= \frac{15}{496}f(j-3) + \frac{1}{248}f(j-2) - \frac{71}{248}f(j-1) \\ &\quad + \frac{1}{2}f(j) - \frac{137}{496}f(j+1) - \frac{1}{248}f(j+2) + \frac{1}{31}f(j+3). \end{aligned} \quad (\text{B2})$$

An example of a typical fit is provided in Fig. 15. As we see, 20% of sites close to each end of the chain are discarded and we only fit the middle part to reduce edge effects. The root mean squared error (‘RMSE’) obtained is $\approx 10^{-5}$.

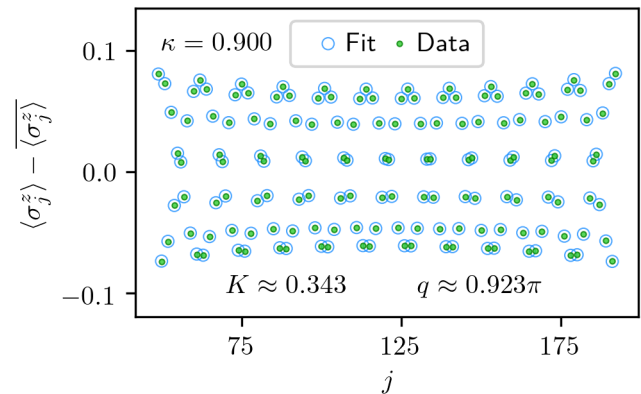


FIG. 15: Extraction of Luttinger liquid parameters from Friedel oscillations profile. This is the Friedel oscillation pattern for $h = 0.5$ inside the floating phase obtained on a finite-size system with $N = 240$ and open boundary conditions. Green points are DMRG data and blue circles are the result of the fit with Eq. 8 (all green points are inside blue circles). Note that the uniform part of the spin density $\overline{\langle \sigma_j^z \rangle}$ has been subtracted, and the fitting window is restricted to the range $j \in [48, 191]$ to avoid edge effects. The root mean squared error (‘RMSE’) obtained is $\approx 10^{-5}$.

-
- [1] S.-H. Lin, R. Dilip, A. G. Green, A. Smith, and F. Pollmann, *PRX Quantum* **2**, 010342 (2021).
 - [2] F. Barratt, J. Dborin, M. Bal, V. Stojevic, F. Pollmann, and A. G. Green, *npj Quantum Information* **7**, 10.1038/s41534-021-00420-3 (2021).
 - [3] W. Huggins, P. Patil, B. Mitchell, K. B. Whaley, and E. M. Stoudenmire, *Quantum Science and Technology* **4**, 024001 (2019).
 - [4] J. Dborin, F. Barratt, V. Wimalaweera, L. Wright, and A. G. Green, *Quantum Science and Technology* **7**, 035014 (2022).
 - [5] M. Rudolph, J. Miller, D. Motlagh, J. Chen, A. Acharya, and A. Perdomo-Ortiz, *Nature Communications* **14** (2023).
 - [6] R. J. Elliott, *Physical Review* **124**, 346 (1961).
 - [7] M. E. Fisher and W. Selke, *Physical Review Letters* **44**, 1502 (1980).
 - [8] W. Selke, *Physics Reports* **170**, 213 (1988).
 - [9] B. K. Chakrabarti, A. Dutta, and P. Sen, *Quantum Ising phases and transitions in transverse Ising models*, Vol. 41 (Springer Science & Business Media, 2008).
 - [10] C. Domb, *Phase transitions and critical phenomena* (Elsevier, 2000).
 - [11] J. Zhang, S. H. Cantú, F. Liu, A. Bylinskii, B. Braverman, F. Huber, J. Amato-Grill, A. Lukin, N. Gemelke, A. Keesling, *et al.*, arXiv preprint arXiv:2401.08087 (2024).
 - [12] W. Selke and M. E. Fisher, *Physical Review B* **20**, 257 (1979).
 - [13] I. Peschel and V. Emery, *Zeitschrift für Physik B Condensed Matter* **43**, 241 (1981).
 - [14] P. Rujan, *Physical Review B* **24**, 6620 (1981).
 - [15] W. Pesch and J. Kroemer, *Zeitschrift für Physik B Condensed Matter* **59**, 317 (1985).
 - [16] D. Allen, P. Azaria, and P. Lecheminant, *Journal of Physics A: Mathematical and General* **34**, L305 (2001).
 - [17] T. Shirahata and T. Nakamura, *Physical Review B* **65**, 024402 (2001).
 - [18] R. Derian, A. Gendiar, and T. Nishino, *Journal of the Physical Society of Japan* **75**, 114001 (2006).
 - [19] A. K. Chandra and S. Dasgupta, *Journal of Physics A: Mathematical and Theoretical* **40**, 6251 (2007).
 - [20] F. Matsubara, T. Shirakura, and N. Suzuki, *Physical Review B* **95**, 174409 (2017).
 - [21] C. Arizmendi, A. Rizzo, L. N. Epele, and C. A. García Canal, *Zeitschrift für Physik B Condensed Matter* **83**, 273 (1991).
 - [22] P. Sen, S. Chakraborty, S. Dasgupta, and B. Chakrabarti, *Zeitschrift für Physik B Condensed Matter* **88**, 333 (1992).
 - [23] H. Rieger and G. Uimin, *Zeitschrift für Physik B Condensed Matter* **101**, 597 (1996).
 - [24] P. Sen, *Physical Review B* **55**, 11367 (1997).
 - [25] A. Dutta and D. Sen, *Physical Review B* **67**, 094435 (2003).
 - [26] M. Beccaria, M. Campostrini, and A. Feo, *Physical Review B* **76**, 094410 (2007).
 - [27] I. Mahyaeh and E. Ardonne, *Physical Review B* **101**,

- 085125 (2020).
- [28] F. K. Fumani, S. Nemati, and S. Mahdaviifar, *Annalen der Physik* **533**, 2000384 (2021).
- [29] A. J. Ferreira-Martins, L. Silva, A. Palhares, R. Pereira, D. O. Soares-Pinto, R. Chaves, and A. Canabarro, arXiv preprint arXiv:2309.15339 (2023).
- [30] A. Nagy, *New Journal of Physics* **13**, 023015 (2011).
- [31] M. Beccaria, M. Campostrini, and A. Feo, *Physical Review B* **73**, 052402 (2006).
- [32] M. D. Grynberg and H. Ceva, *Physical Review B* **36**, 7091 (1987).
- [33] P. R. C. Guimaraes, J. A. Plascak, F. C. S. Barreto, and J. Florencio, *Physical Review B* **66**, 064413 (2002).
- [34] S. Monaco, O. Kiss, A. Mandarino, S. Vallecorsa, and M. Grossi, *Physical Review B* **107**, 10.1103/physrevb.107.1081105 (2023).
- [35] M. C. Caro, H.-Y. Huang, M. Cerezo, K. Sharma, A. Sornborger, L. Cincio, and P. J. Coles, *Nature communications* **13**, 4919 (2022).
- [36] R. Orús, *Annals of physics* **349**, 117 (2014).
- [37] N. Schuch, arXiv preprint arXiv:1306.5551 (2013).
- [38] J. Eisert, arXiv preprint arXiv:1308.3318 (2013).
- [39] R. Augusiak, F. Cucchietti, and M. Lewenstein, in *Modern Theories of Many-Particle Systems in Condensed Matter Physics* (Springer, 2012) pp. 245–294.
- [40] F. Verstraete, V. Murg, and J. I. Cirac, *Advances in physics* **57**, 143 (2008).
- [41] J. I. Cirac and F. Verstraete, *Journal of physics a: mathematical and theoretical* **42**, 504004 (2009).
- [42] J. Biamonte and V. Bergholm, arXiv preprint arXiv:1708.00006 (2017).
- [43] S. Montangero, E. Montangero, and Evenson, *Introduction to tensor network methods* (Springer, 2018).
- [44] P. Silvi, F. Tschirsich, M. Gerster, J. Jünemann, D. Jaschke, M. Rizzi, and S. Montangero, *SciPost Physics Lecture Notes*, 008 (2019).
- [45] S. Montangero, E. Rico, and P. Silvi, *Philosophical Transactions of the Royal Society A* **380**, 20210065 (2022).
- [46] S.-J. Ran, E. Tirrito, C. Peng, X. Chen, L. Tagliacozzo, G. Su, and M. Lewenstein, *Tensor Network Contractions: Methods and Applications to Quantum Many-Body Systems* (Springer Nature, 2020).
- [47] M. C. Bañuls, *Annu. Rev. Condens. Matter Phys.* **14**, 173 (2023).
- [48] E. M. Stoudenmire, *Quantum Science and Technology* **3**, 034003 (2018).
- [49] D. Liu, S.-J. Ran, P. Wittek, C. Peng, R. B. García, G. Su, and M. Lewenstein, *New Journal of Physics* **21**, 073059 (2019).
- [50] Z.-Y. Han, J. Wang, H. Fan, L. Wang, and P. Zhang, *Physical Review X* **8**, 031012 (2018).
- [51] S. R. White, *Physical review letters* **69**, 2863 (1992).
- [52] S. R. White, *Physical review b* **48**, 10345 (1993).
- [53] S. Östlund and S. Rommer, *Physical review letters* **75**, 3537 (1995).
- [54] F. Verstraete, D. Porras, and J. I. Cirac, *Physical review letters* **93**, 227205 (2004).
- [55] A. J. Daley, C. Kollath, U. Schollwöck, and G. Vidal, *Journal of Statistical Mechanics: Theory and Experiment* **2004**, P04005 (2004).
- [56] U. Schollwöck, *Reviews of modern physics* **77**, 259 (2005).
- [57] U. Schollwöck, *Annals of physics* **326**, 96 (2011).
- [58] Y. Levine, O. Sharir, N. Cohen, and A. Shashua, *Physical review letters* **122**, 065301 (2019).
- [59] M. Qin, T. Schäfer, S. Andergassen, P. Corboz, and E. Gull, *Annual Review of Condensed Matter Physics* **13**, 275 (2022).
- [60] M. Frías-Pérez, L. Tagliacozzo, and M. C. Bañuls, *Converting long-range entanglement into mixture: Tensor-network approach to local equilibration* (2023), arxiv:2308.04291 [cond-mat, physics:quant-ph].
- [61] M. Fannes, B. Nachtergaele, and R. F. Werner, *Communications in mathematical physics* **144**, 443 (1992).
- [62] A. Klümper, A. Schadschneider, and J. Zittartz, *Journal of Physics A: Mathematical and General* **24**, L955 (1991).
- [63] A. Klümper, A. Schadschneider, and J. Zittartz, *Europhysics Letters* **24**, 293 (1993).
- [64] M. B. Hastings, *Physical review b* **73**, 085115 (2006).
- [65] M. B. Hastings, *Journal of statistical mechanics: theory and experiment* **2007**, P08024 (2007).
- [66] L. Tagliacozzo, G. Evenbly, and G. Vidal, *Physical Review B* **80**, 235127 (2009).
- [67] S. Yan, D. A. Huse, and S. R. White, *Science* **332**, 1173 (2011).
- [68] S. R. White, *Annu. Rev. Condens. Matter Phys.* **3**, 111 (2012).
- [69] B.-X. Zheng, C.-M. Chung, P. Corboz, G. Ehlers, M.-P. Qin, R. M. Noack, H. Shi, S. R. White, S. Zhang, and G. K.-L. Chan, *Science* **358**, 1155 (2017).
- [70] H.-C. Jiang and T. P. Devereaux, *Science* **365**, 1424 (2019).
- [71] M. Qin, C.-M. Chung, H. Shi, E. Vitali, C. Hubig, U. Schollwöck, S. R. White, S. Zhang, *et al.*, *Physical Review X* **10**, 031016 (2020).
- [72] J. L. Cardy, *J. Phys. A: Math. Gen.* **17**, L385 (1984).
- [73] C. Holzhey, F. Larsen, and F. Wilczek, *Nuclear physics b* **424**, 443 (1994).
- [74] G. Vidal, J. I. Latorre, E. Rico, and A. Kitaev, *Physical review letters* **90**, 227902 (2003).
- [75] J. I. Latorre, E. Rico, and G. Vidal, arXiv preprint quant-ph/0304098 (2003).
- [76] P. Calabrese and J. Cardy, *Journal of statistical mechanics: theory and experiment* **2004**, P06002 (2004).
- [77] T. Nishino, K. Okunishi, and M. Kikuchi, *Physics Letters A* **213**, 69 (1996).
- [78] L. Tagliacozzo, Thiago. R. de Oliveira, S. Iblisdir, and J. I. Latorre, *Phys. Rev. B* **78**, 024410 (2008).
- [79] F. Pollmann, S. Mukerjee, A. M. Turner, and J. E. Moore, *Phys. Rev. Lett.* **102**, 255701 (2009).
- [80] M. Henkel, *Conformal invariance and critical phenomena* (Springer Science & Business Media, 1999).
- [81] M. E. Fisher and M. N. Barber, *Physical Review Letters* **28**, 1516 (1972).
- [82] K. Binder, D. W. Heermann, and K. Binder, *Monte Carlo simulation in statistical physics*, Vol. 8 (Springer, 1992).
- [83] T. Giamarchi, *Quantum physics in one dimension*, Vol. 121 (Clarendon press, 2003).
- [84] J. Hauschild and F. Pollmann, *SciPost Physics Lecture Notes*, 005 (2018).
- [85] V. Dunjko and H. J. Briegel, *Reports on Progress in Physics* **81**, 074001 (2018).
- [86] Y. Liu, S. Arunachalam, and K. Temme, *Nature Physics*, 1 (2021).

- [87] C. Gyurik and V. Dunjko, arXiv:2208.06339 , (2022).
- [88] J. R. McClean, S. Boixo, V. N. Smelyanskiy, R. Babush, and H. Neven, Nat. Commun. **9**, 4812 (2018), arXiv:1803.11173 [quant-ph].
- [89] M. S. Rudolph, S. Lerch, S. Thanasilp, O. Kiss, S. Vallecorsa, M. Grossi, and Z. Holmes, arXiv:2305.02881 , (2023).
- [90] L. Bittel and M. Kliesch, Phys. Rev. Lett. **127**, 120502 (2021).
- [91] M. Cerezo, M. Larocca, D. García-Martín, N. L. Diaz, P. Braccia, E. Fontana, M. S. Rudolph, P. Bermejo, A. Ijaz, S. Thanasilp, E. R. Anschuetz, and Z. Holmes, Does provable absence of barren plateaus imply classical simulability? or, why we need to rethink variational quantum computing (2023), arXiv:2312.09121 [quant-ph].
- [92] I. Cong, S. Choi, and M. D. Lukin, Nat. Phys. **15**, 1273–1278 (2019).
- [93] M. Cerezo, A. Sone, T. Volkoff, L. Cincio, and P. J. Coles, Nature communications **12**, 1791 (2021).
- [94] A. Pesah, M. Cerezo, S. Wang, T. Volkoff, A. T. Sornborger, and P. J. Coles, Phys. Rev. X **11**, 041011 (2021).
- [95] F. Hua, Y. Jin, Y. Chen, S. Vittal, K. Krsulich, L. S. Bishop, J. Lapeyre, A. Javadi-Abhari, and E. Z. Zhang, Exploiting qubit reuse through mid-circuit measurement and reset (2023), arXiv:2211.01925 [quant-ph].
- [96] K. Chinzei, Q. H. Tran, K. Maruyama, H. Oshima, and S. Sato, Splitting and parallelizing of quantum convolutional neural networks for learning translationally symmetric data (2023), arXiv:2306.07331 [quant-ph].
- [97] R. Verresen, A. Vishwanath, and F. Pollmann, arXiv preprint arXiv:1903.09179 (2019).
- [98] N. Chepiga and F. Mila, Physical Review B **107**, L081106 (2023).
- [99] S. Sachdev, Physics world **12**, 33 (1999).
- [100] T. Shirakura, F. Matsubara, and N. Suzuki, Physical Review B **90**, 144410 (2014).
- [101] V. Pokrovsky and A. Talapov, Physical Review Letters **42**, 65 (1979).
- [102] S. Suzuki, J.-i. Inoue, and B. K. Chakrabarti, *Quantum Ising phases and transitions in transverse Ising models*, Vol. 862 (Springer, 2012).
- [103] P. Bak, Reports on Progress in Physics **45**, 587 (1982).
- [104] D. A. Huse and M. E. Fisher, Physical Review B **29**, 239 (1984).
- [105] F. Haldane, Journal of Physics C: Solid State Physics **14**, 2585 (1981).
- [106] J. L. Cardy and D. C. Lewellen, Physics Letters B **259**, 274 (1991).
- [107] S. R. White, I. Affleck, and D. J. Scalapino, Physical Review B **65**, 165122 (2002).
- [108] M. Fabrizio and A. O. Gogolin, Physical Review B **51**, 17827 (1995).
- [109] N. Chepiga and F. Mila, Physical Review Research **3**, 023049 (2021).
- [110] G. Dzhaparidze and A. Nersesyan, Soviet Journal of Experimental and Theoretical Physics Letters **27**, 334 (1978).
- [111] I. Affleck and A. W. Ludwig, Physical Review Letters **67**, 161 (1991).
- [112] P. Calabrese and J. Cardy, Journal of physics a: mathematical and theoretical **42**, 504005 (2009).
- [113] N. Chepiga, I. Affleck, and F. Mila, Physical Review B **101**, 174407 (2020).
- [114] A. Peruzzo, J. McClean, P. Shadbolt, M.-H. Yung, X.-Q. Zhou, P. J. Love, A. Aspuru-Guzik, and J. L. O’Brien, Nature Communications **5**, 4123 (2014).
- [115] M. S. Rudolph, J. Chen, J. Miller, A. Acharya, and A. Perdomo-Ortiz, Quantum Science and Technology **9**, 015012 (2023).
- [116] K. Kottmann, F. Metz, J. Fraxanet, and N. Baldelli, Phys. Rev. Research **3**, 043184 (2021).
- [117] J. Dborin, F. Barratt, V. Wimalaweera, L. Wright, and A. G. Green, Quantum Science and Technology **7**, 035014 (2022).
- [118] L. Ornstein and F. Zernike, Koninklijke Nederlandsche Akademie van Wetenschappen Proceedings **19**, 1312 (1914).
- [119] E. S. Sørensen, M.-S. Chang, N. Laflorencie, and I. Affleck, Journal of Statistical Mechanics: Theory and Experiment **2007**, P08003 (2007).